Computational Design of Metal-Exchanged MFI Zeolites for Coupling CO_2─Ethylene to Form Acrylic Acid

Zaheer Masood, Quy P. Nguyen, Bin Wang *

School of Sustainable Chemical, Biological and Materials Engineering, University of Oklahoma, Norman, Oklahoma 73019, United States

Email: Wang_cbme@ou.edu

Abstract

The production of acrylic acid by coupling CO_2 and ethylene is highly desirable as it uses a C1 molecule to introduce the carboxylic group into a large commodity chemical, forming an unsaturated carboxylic acid. Molecular complexes have been used as catalysts in the literature for this reaction; however, these homogeneous studies were all limited by low activity and stability, and efficient heterogeneous catalysts remain to be explored. Here, we report density functional theory calculations, through which we investigated metal-exchanged MFI zeolites with metals from 3d, 4d and 5d series for this reaction. Screening of reaction thermodynamics has shown that Sc, Y, Cr, Mo, W, Mn, Tc and Re dispersed into MFI zeolites are potential catalysts. We further calculated the activation barriers for the β─H transfer, a key elementary step that normally determines the overall rates, and found the lowest barrier over Sc- and Y-MFI; such a feasible kinetics is attributed to the low electronegativity of Sc and Y that strongly affects the nature of the transition states and the charge redistribution during the β─H transfer. This work thus provides guidelines for designing a zeolite-based catalyst for this valuable reaction and identifies promising metal centers to be used.

Keywords: Carboxylation, metallalactone, zeolites, DFT, hydrogen transfer

Introduction

Acrylic acid and its derivatives are widely used in the manufacturing of a variety of chemicals and materials. For example, acrylic acid is used in the production of polyacrylic acid and polymethyl methacrylate with applications in the automotive, construction, and packaging industries. Acrylic acid derivatives are high-value, high-volume building blocks for plastics, absorbents, coatings, adhesives, paints, and textiles.[1-3] The market of acrylic acid is forecast to reach USD 19.92 billion in 2030. [4] Currently, acrylic acid is commercially produced by the two-step oxidation of propane with O_2 via acrolein as the intermediate. [5-6] This process is energy-intensive, resulting in significant CO_2 emissions, and requires expensive catalysts and harsh reaction conditions. Instead, acrylic acid and its derivatives can be produced via one-step fermentation, but the efficiency is low. [7] Catalytic dehydration of biomass-derived methyl lactate to acrylic acid is another alternate route, but it is still a challenge to reach high selectivity and production rates. [8]

The utilization of CO_2, a major greenhouse gas, as one-carbon (C_1) building block in chemical synthesis is very appealing for a sustainable carbon economy. [9-17] Synthesis of acrylic acid from ethylene and CO_2 is one of the examples. As ethylene can potentially be generated from electrochemical reduction of CO_2, [18] a synthesis route based solely on CO_2 to produce acrylic acid is thus possible and highly desirable. However, cooperative activation and coupling of CO_2 with ethylene to form acrylic acid requires well-designed catalysts to achieve this energy- and atom-efficient conversion. Extensive efforts have been made for CO_2─ethylene coupling to synthesize acrylic acid, and computational studies have been performed to explore reaction mechanisms on

organometallic complexes with Ni, Pd, W, Mo, Fe, Pt, Ru and Rh as metal centers.[1, 19-24] It has been accepted that the reaction starts with co-adoption of CO_2 and ethylene on the metal center, forming a metallalactone (five-membered ring) intermediate. Transfer of H from β-carbon (β─H) to O in the metallalactone ring results in the formation of adsorbed acrylic acid, the desorption of which regenerates the complex/catalyst. [1-2, 25] There are several studies of CO_2 coupling with different olefins (including C_2H_4) with a focus on the selection of the metal centers and ligand design but all with low activity and stability manifested by a very low turnover number (TON) [20, 26-31], which is caused by the high free energy barriers for metallalactone formation and slow kinetics of the β─H elimination. The loss of catalytic activity was also observed due to the dimerization of the molecular catalysts. In addition, most of these prior studies are stoichiometric reactions, rather than catalytic reactions, and require harsh reaction conditions. [1-2, 32] Therefore, it is valuable to design well-defined active sites in heterogeneous catalysts, which can potentially increase the process efficiency of CO_2─ethylene coupling under mild reaction conditions.

Design of a heterogenous catalysis process can enhance conversion efficiency by increasing the density of active sites to promote the rate and reducing separation cost, both of which are highly desirable for industrial applications. Despite several experimental and computational efforts, active and robust heterogeneous catalysts are yet to be discovered. [22-23] Metal-exchanged zeolite offers atomically dispersed metal atoms with fine tunability of the electronic properties of the active sites for binding and activating CO_2 and ethylene. The well-defined microporosity may also stabilize the bulky transition states and reaction intermediates.[33-36] In addition, metal-exchanged zeolites have been reported to catalyze the coupling between CO_2 and CH_4 to form acetic acid,[37-39] but their feasibility for CO_2─ethylene coupling remains to be explored.

Therefore, in this work, we chose metal-exchanged MFI zeolites with atomically dispersed active sites for CO_2─ethylene coupling to synthesize acrylic acid. We report density functional theory (DFT) studies, through which we investigated atomically dispersed transition metals from 3d, 4d and 5d series for CO_2─ethylene coupling. First, we screened possible catalyst materials based on reaction free energies for CO_2─ethylene coupling to form acrylic acid. Our initial thermodynamic screening showed that Sc, Y, Cr, Mo, W, Mn, Tc and Re dispersed in MFI zeolites could be possible catalytic active sites. Then, these metal centers were investigated for a detailed kinetic study of the β─H transfer step, which is likely the rate-limiting step as highlighted by previous literature studies on molecular catalysts. [31-32, 40] Our results show that the β─H transfer can be achieved with a moderate activation barrier (120 to 140 kJ/mol) over Sc, Y, and Mn dispersed in MFI zeolite. Furthermore, we show that the β─H transfer barrier is proportional to the electronegativity of the metal center. This work thus provides valuable guidelines for designing the zeolite-based active sites for this CO_2─ethylene coupling reaction.

Computational Methods

All DFT calculations with projector augmented wave (PAW) [41-42] potentials and the Perdew-Burke-Ernzerhof (PBE) exchange and correlation functional [43] were performed using the Vienna ab-initio simulation package (VASP)[44]. The unit cell of H-ZSM-5 was used in all calculations, and it included 96 T atoms (T = Si, Al) and 192 oxygen atoms. The lattice constants of MFI unit cell are a = 20.078 Å, b = 19.894 Å, c = 13.372 Å, which were taken from experimental work [45] and used in our previous works. [46-47] The structural relaxation was carried out using a single Γ point of Brillouin zone with a planewave kinetic cutoff energy of 400 eV. Either the quasi-Newton scheme or the conjugate gradient algorithm implemented in VASP was used for geometry optimization until the forces of each atom were converged to less than 0.02 eV $Å^{-1}$. The electronic

self-consistency cycles were converged to < 10^{-6} eV with Gaussian smearing of 0.02 eV. The Grimme dispersion (DFT-D3) correction with zero damping function [48-49] was used to account for the contribution of the van der Waals interactions. Transition state calculations were carried out using the climbing image nudged elastic band (NEB) method with six intermediate images [50]. Transition states were refined by the dimer calculations [51] and confirmed by the single imaginary frequency from vibrational calculations.

Free energies of all intermediates were determined using $G^\circ = E^\circ_{elect} - TS + ZPE$, where E°_{elect} was obtained from the DFT calculations, and TS (T = 298 K) and ZPE (zero-point energy) were calculated from the harmonic frequencies of the adsorbed, and gaseous species at the standard states. The VASPKIT package was used to calculate ZPE and entropy contributions.[52] In frequency calculations of adsorbed states, all atoms in adsorbates and active ensemble (the transition metal atom, two Al atoms, two oxygens bridging Al and Si and one Si atom as shown in in Figure 1c,d) were allowed to move. Other atoms in MFI were frozen at their optimized positions. We also compared entropic contributions using the free-rotor approximation [53] and found a negligible energy difference (0.12 kJ/mol) between the two approaches. We also validated our results with spin-polarized calculations on Sc-MFI by calculating the intrinsic barriers for the hydrogen-transfer step using the initial, transition, and final states structures obtained through the non-spin-polarized calculations. The difference in the calculated intrinsic activation barriers (~ 4 kJ/mol) is not significant as compared to the absolute value, which is about 120 kJ/mol. Therefore, in the discussion below, only the results from non-spin-polarized calculations are included.

To prepare the structures, in MFI zeolite two Si^{4+} atoms at T-sites T5 and T9 were replaced with two Al^{3+} atoms, which results in two negative charges distributed on adjacent oxygen atoms. These positions were selected because the formed metal center is accessible to the reactants and

products through straight and sinusoidal channels of MFI zeolites. The oxidation states of metal centers are determined by the number of substitutional Al in the framework, so in this way we maintain a similar oxidation state of metal centers by positioning them with the same configurations (Figure 1a-c). It should be noted that the oxidation state of the metal center can be modified in experimental synthesis (e.g., different Si/Al ratio and Al distribution) and evolve under reaction conditions by interacting with ligands such as OH; however, detailed calculations of reaction profiles over all possible oxidation states for each metal center demand significant computational resources and time and are beyond the scope of this work. Instead, the approach in this work allows us to screen the metal and derive theoretical trends of the reaction profile as a function of the electronic structure of the metal centers. We constructed a model active site that is located at the intersection and accessible to molecular reactants. The intersection, compared with the straight and sinusoidal channels, have less steric hinderance for reaction intermediates. We expect, depending on the exact location of the mental centers in the microporous structure, the stability of the intermediate species and transition states may change; however, the conclusion on the trend of the reaction profile over different metal centers likely remain, as the confinement to different metal centers offered by the microporous structure could cancel out.

Results and discussion

Atomically dispersed active sites within MFI zeolites can be formed by controlling metal loading and distribution of the framework Al atoms. [54-55] In the calculations reported here, we assume the metals are cations positive charges. The model of active site in the MFI framework is shown in **Figure 1a-c**. We included all the 3d and 4d transition metals and W, Re and Ir from 5d transition metals as cations dispersed in the MFI porous structure. Investigated metals are shown

in the bottom part of **Figure 1**. The different metals are expected to cause different stabilities of reaction intermediates, resulting in varied free energy profiles, and hence regulating the performance of the catalysts.

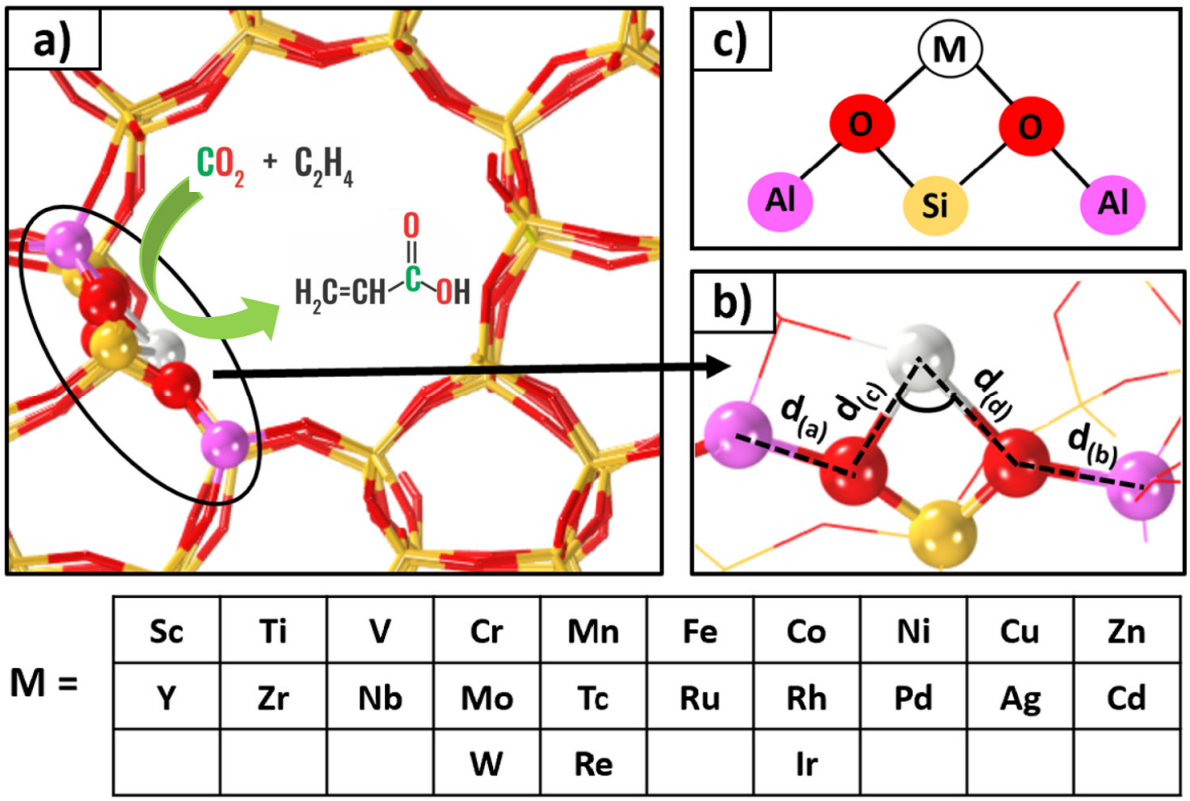

M =

Sc	Ti	V	Cr	Mn	Fe	Co	Ni	Cu	Zn
Y	Zr	Nb	Mo	Tc	Ru	Rh	Pd	Ag	Cd
			W	Re		Ir			

Figure 1. Structural models for the metal-exchanged ZSM-5. (a) O–M–O active site model (atomically dispersed metal) in MFI Zeolite, (b) magnified O–*M–O active site and (c) sketch of O–*M–O active site (M is transition metal) and * represents MFI zeolite.

The coupling of $CO_{2(g)}$ and $C_2H_{4(g)}$ to form acrylic acid was investigated using the reaction scheme presented in **Figure 2**. The reaction can take place either from the adsorption of C_2H_4 to form *M─C_2H_4 via step (i) or the adsorption of CO_2 to form CO_2-adduct (*M─CO_2) via step (ii) (* on transition metal represents metal-exchanged MFI zeolite). In the next steps, the formation of metallalactone (five-member ring) can happen via step (iii) or step (iv). We adapted the inner sphere pathway for metallalactone formation because the inner sphere pathway is favorable over the outer sphere as demonstrated by Al-Ghamdi M. et al.[25] Further, the transfer of β─H to O in

metallalactone results in the formation of adsorbed acrylic acid. The active site is regenerated either by ligand exchange (with C_2H_4), step (vi), or the desorption of acrylic acid, step (vii).

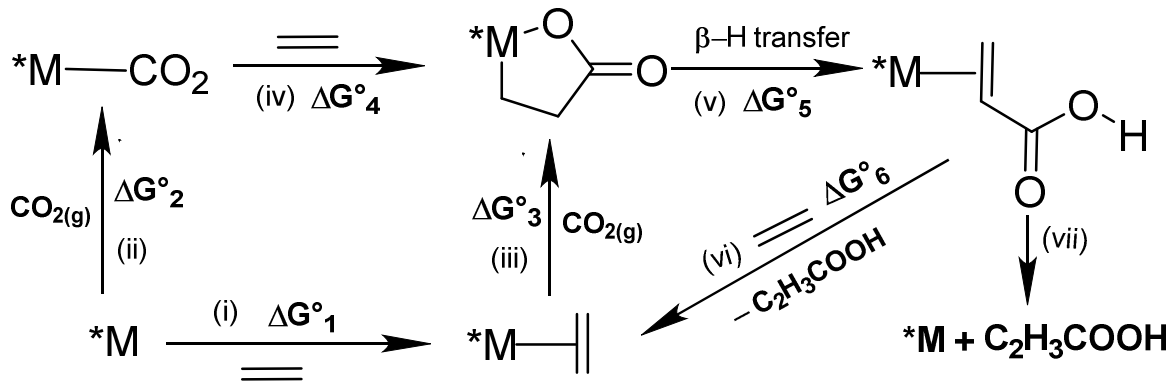

Figure 2. Reaction mechanism of coupling $CO_{2(g)}$ and $C_2H_{4(g)}$ to form acrylic acid used in this study. M* represents metal ion in MFI zeolite.

Before further screening of the metal centers for potential active sites, a favorable pathway for metallalactone formation was determined. The metallalactone forms either via steps (i) and (iii) or steps (ii) and (iv), depending on the adsorption free energies of ethylene or CO_2, respectively. The computed free energies of adsorption of $C_2H_{4(g)}$ and $CO_{2(g)}$ are presented in **Figure 3**. $C_2H_{4(g)}$ is bound to the metal via d-π interaction. **Figure 3** shows that the adsorption free energies of $C_2H_{4(g)}$ are more negative, that is more thermodynamically favorable than those of $CO_{2(g)}$ on all *M except *Zr. During structural optimization, *Zr─CO_2 dissociated into *Zr─CO and *Zr─O, likely caused by the high oxophilicity of the metal. Zr-ZSM5 was thus not investigated in the following as we wanted to introduce the carboxylic group into the final product. Additionally, all adsorption free energies are negative (thermodynamically favorable) except $CO_{2(g)}$ binding with *Co. Overall, **Figure 3** indicates that the adsorption of $C_2H_{4(g)}$ is always more favorable than the binding of $CO_{2(g)}$ (step (i) is dominant over step (ii)). That is, the reaction is expected to proceed via step (i) and step (iii) for the formation of metallalactone on these catalysts.

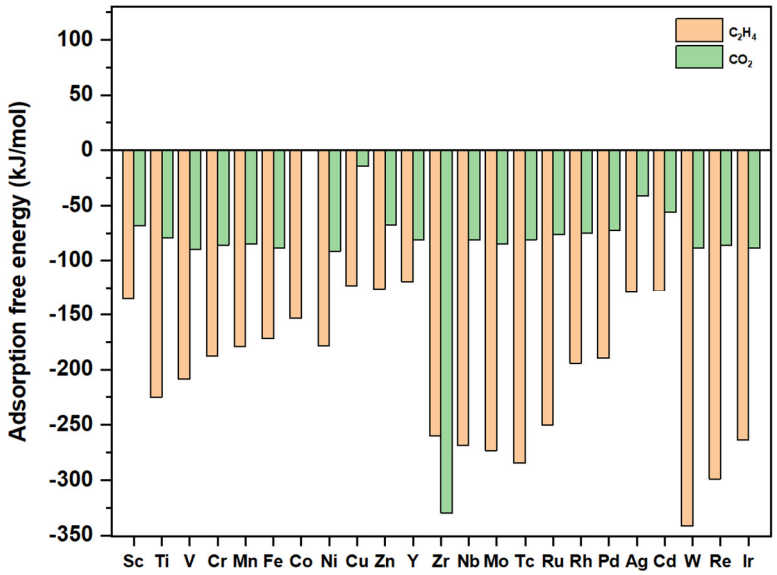

Figure 3. Adsorption free energies of $CO_{2(g)}$ (brown bars) and $C_2H_{4(g)}$ (green bars) on *M. The reference is the gas phase molecules and metal-exchanged MFI.

Reaction free energies for step (i) C_2H_4 adsorption (ΔG°_1), step (iii) C-C coupling (ΔG°_3) and step (v) hydrogen transfer (ΔG°_5) according to the scheme shown in **Figure 2** are presented in **Table 1**. All positive reaction free energies are tagged with the § sign. Based on the reaction free energies, potential active sites can be classified into three categories based on reaction free energies (ΔG°). (1) metallalactone formation is less favorable due to positive ΔG°_3, (2) hydrogen (β─H) transfer step (v) is less favorable due to positive ΔG°_5, and (3) reaction free energies for all steps are negative or slightly positive. In this (1) class of catalysts, the formation of the five-membered ring is unfavorable. Unfavorable formation of the metallalactone intermediate is either indicated by the dissociation of the five-membered ring to *M─CO_2 and *M─C_2H_4 or by positive reaction free energies of the ring formation step. On *Cu, *Zn, *Ag, and *Cd, the five-membered ring dissociates to *M─CO_2 and *M─C_2H_4 during structural optimization. On these atomic sites, the formation of metallalactone is kinetically relevant. Within this category, energy differences for metallalactone formation are between 49.2 (*Co) and 153.4 kJ/mol (*Pd), including 67.5 on *Ru,

69.5 on *Rh, 67.5 on *Ir, and 118.7 kJ/mol on *Ni. A previous study by Graham D. C. et al. also reported the reaction free energy of 121.8 kJ/mol using DFT calculations for the formation of nickelalactone, [40] which is very close to our calculated value of 118.7 kJ/mol for *Ni-MFI. The free energy profile of $CO_{2(g)}$ coupling with $C_2H_{4(g)}$ on *Ru, *Co, *Rh, *Ir, *Ni and *Pd are presented in **Figure S1** (Supplementary Information). We anticipate that the uphill thermodynamics for the metallalactone formation restricts the overall reaction profile and that these metal-exchanged MFI are not desirable for catalyzing the coupling reaction; we thus didn't consider these metal-exchanged MFI in the calculations of kinetics.

For the next class of catalysts, **Table 1** shows that ΔG°_5 for the β─H transfer step is the positive on *Ti, *V, *Nb and *Fe. The free energy change ΔG°_5 for β–H transfer ranges from 39.6 kJ/mol on *V to 81.1 kJ/mol on *Ti. Here, on *Fe, ΔG°_3 of metallalactone formation is also positive, but ΔG°_5 (41.5 kJ/mol) is slightly greater than ΔG°_3, allowing us to include *Fe in this category. Free energy profiles of $CO_{2(g)}$ coupling with $C_2H_{4(g)}$ on *Ti, *V, *Nb and *Fe are presented in **Figure S2** (Supplementary Information). This unfavorable thermodynamics for β─H transfer over *Ti, *V, *Nb, and *Fe is caused by the strong metal-oxygen bonds, a result of the high oxophilicity of the metal centers, which inhibits the hydrogen transfer to the oxygen that breaks the strong metal-oxygen bonds.

In the following, we focus our discussion on the third category where all steps are negative or slightly positive. That is, over transition metals in this category, the reaction is more thermodynamically favorable. **Table 1** shows that all reaction free energies are negative on *Sc, *Y, *Cr, *Mo, *W, *Tc and *Re. The Mn-MFI has a slightly positive ΔG°_3 but is included in this category due to the small free energy difference. Free energy profiles of $CO_{2(g)}$ coupling with $C_2H_{4(g)}$ on *Sc, *Y, *Cr, *Mo, *W, *Tc and *Re are presented in **Figure S3**. These results show

that among all candidates tested, *Sc, *Y, *Cr, *Mo, *W, *Tc, *Mn, and *Re can be potential candidates for CO_2─ethylene coupling based on this thermodynamic screening.

The detailed analysis of the structures of the catalysts **(Table S1)**, *C_2H_4 (**Figure S4(a-h)**), and metallalactone (**Figure S4(i-p)**) are presented in Section S1 of the Supplementary Information. The metallalactone ring formation was investigated by the reaction of $CO_{2(g)}$ with pre-adsorbed *C_2H_4 following the Eley-Rideal mechanism [56-57]. Reaction free energies for this step are between -67.5 (*Sc) and 8.7 (*Mn), and other metal centers like *Y (-44.4), *Cr (-39.6), *Mo (-57.9), *W (-47.3), *Tc (-56.0), and *Re (-22.2) kJ/mol are within this range. Optimized structures of metallalactone are presented in **Figure S4(i-p)** in the Supplementary Information. We found strong correlations of free energies of *C_2H_4, metallalactone, and *C_2H_5COOH and presented in **Figure S5a** and **b**. The detailed analysis of β─H transfer from metallalactone to form acrylic acid will be discussed below as it is a key elementary step responsible for the formation of adsorbed acrylic acid or acrylate [31-32, 40].

Table 1. Reaction free energies in kJ/mol for step (i) (ΔG°_1) C_2H_4 adsorption, step (iii) (ΔG°_3) metallalactone formation and step (v) (ΔG°_5) hydrogen transfer according to **Figure 2**.

M	ΔG°_1	ΔG°_3	ΔG°_5
*Sc	-135.1	-67.5	-3.9
*Ti	-224.8	-115.8	81.1§
*V	-208.4	-132.2	39.6§
*Cr	-187.2	-39.6	-13.5
*Mn	-178.5	8.7§	-34.7
*Fe	-171.7	39.6§	41.5§
*Co	-153.4	49.2§	22.2§
*Ni	-178.5	118.7§	-42.5
*Cu	-122.8	--	--
*Zn	-125.7	--	--
*Y	-118.7	-44.4	-43.4
*Nb	-268.2	-128.3	61.8§
*Mo	-273.1	-57.9	-16.4
*Tc	-81.1	-56.0	-17.4
*Ru	-249.9	67.5§	25.1§
*Rh	-193.9	69.5§	16.4§
*Pd	-190.1	153.4§	-62.7
*Ag	-129.5	--	--
*Cd	-127.6	--	--
*W	-341.6	-47.3	-3.9
*Re	-299.1	-22.2	-4.8
*Ir	-236.4	67.5*	40.5§

§ indicates positive free energies

The reaction free energies of the β─H transfer from C to O to form acrylic acid, ΔG°_5, are found most thermodynamically favorable over *Y (-43.4 kJ/mol) and *Mn (-34.7 kJ/mol), followed by *Tc (-17.4), *Mo (-16.4), *Cr (-13.5), *Re (-4.8), *Sc (-3.9) and *W (-3.9). Reaction

free energies of the β─H transfer are all negative within this category of metal centers. Previous studies show β─H transfer is the rate-limiting step, resulting in low TON of acrylic acid or acrylates. [31-32, 40] Therefore, in the following, beyond the thermodynamic calculations, we calculated the activation energies for this β─H transfer.

The energies of activation (E_{act}) for β─H transfer vary by ~ 70 kJ/mol, ranging from 119.6 (*Sc) to 193.0 kJ/mol (*W), including 129.3 over *Y, 139.9 over *Mn, 168.8 over *Cr, 177.5 over *Tc, 181.4 over *Mo, and 188.1 over *Re . The free energy profiles of $CO_{2(g)}$ coupling with $C_2H_{4(g)}$ to form adsorbed acrylic acid are presented in **Figure 4a,b**. **Figure 4** shows that adsorbates are loosely bonded with *Sc, *Tc, and *Y, moderately bonded with *Mn and *Cr, while strongly bonded with *Re, *W and *Mo. The relatively strong adsorption of adsorbates also indicates significant metal-ligand interaction. This strong interaction stabilizes the intermediate species, such as the metallalactone, but suppresses the hydrogen transfer kinetics. Based on E_{act} for the β─H transfer, the reaction kinetics to form acrylic acid follows the trend: *Sc > *Y > *Mn > *Cr > *Tc > *Mo > *Re > *W. Particularly, the Sc, Y and Mn centers show the lower barriers for hydrogen transfer; the activation barrier generally follows the trend of the bonding strength. That is, too strong interaction between the adsorbates and the metal centers inhibits the hydrogen transfer, which needs to break metal-ligand bonds.

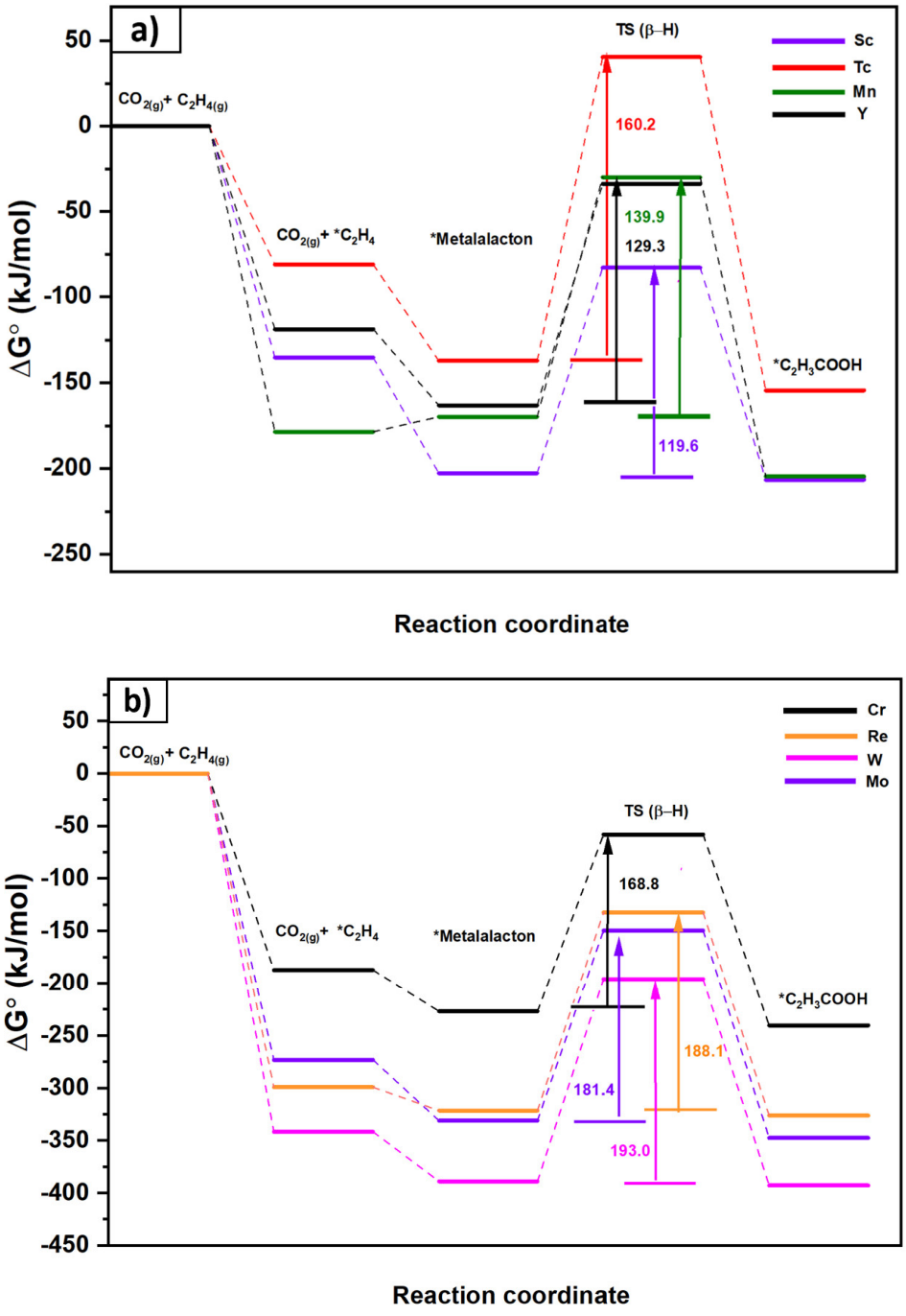

Figure 4. Free energy profile of CO_2 coupling with C_2H_4 to form acrylic acid on (a) *Sc, *Tc, *Mn and *Y (b) *Cr, *Re, *W and *Mo. The activation barrier for the hydrogen transfer step is highlighted.

In the following, we discuss the physical reasons based on electronic structure calculations to explain the calculated activation energy values of the hydrogen transfer step. **Figure 5(a)** shows

the activation energy (E_{act}) vs. the reaction energy for the β─H transfer step. This plot is linear following the Brønsted−Evans−Polanyi (BEP) relation, [58] except *Sc .

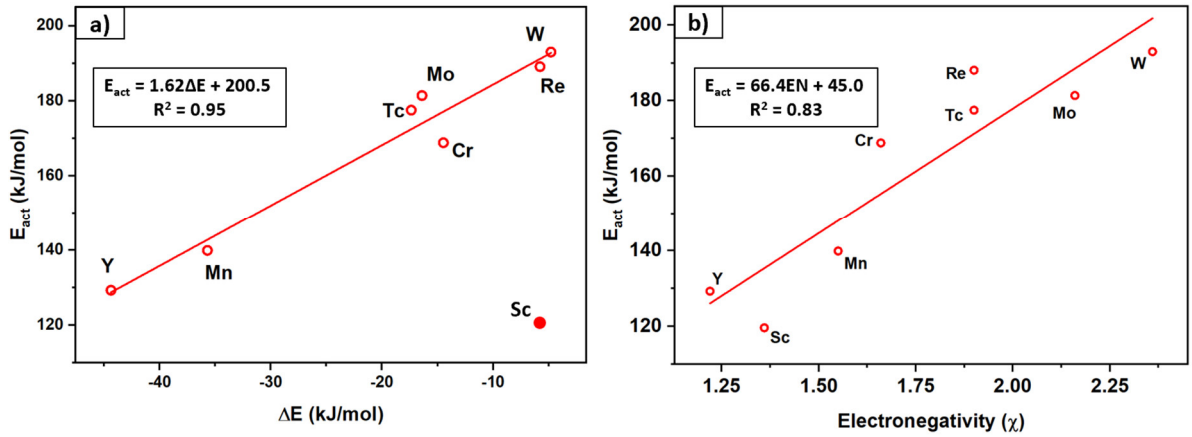

Figure 5. Physical reason that determines the activation barrier. (a) Plot of E_{act} vs. ΔE for proton transfer from C to O (β─H transfer) (Sc is not included in regression) and (b) correlation of E_{act} with electronegativity of the metal atom.

To understand the origin of the deviation of *Sc from the linear trend in **Figure 5(a),** we conducted the structural analysis of the transition states. The geometries of transition states of all catalysts (side and top view) within this category are presented in **Figure 6(a-h)**. All transition states are similar in atomic structures; in these transition states, the proton is approximately in the middle of C and O atoms and no major difference is noted. To investigate further, we conducted the projected density of states (PDOS) analysis of the metal center and C (bearing β─H) in transition states (**Figure S6**), which shows a small overlap of PDOS between Sc (and Y) and C in the range of -2 to -6 eV. This lack of orbital overlapping suggests a weaker metal-carbon interaction, which is also in line with the weaker adsorption energy (**Figure 4**) and longer M-C bond (shown by the blue dashed line in **Figure 6**) over *Sc (2.53 Å) and *Y (2.78 Å). The Sc-C and Y-C bond length is greater than M─C bond in other transition state structures in **Figure 6(c-**

h), which is 2.14 ± 0.04 Å. This elongated M-C bond is also observed for ethylene adsorption shown in **Figure S4(a-h)**, distinguishing Sc and Y from the rest of the tested metal centers.

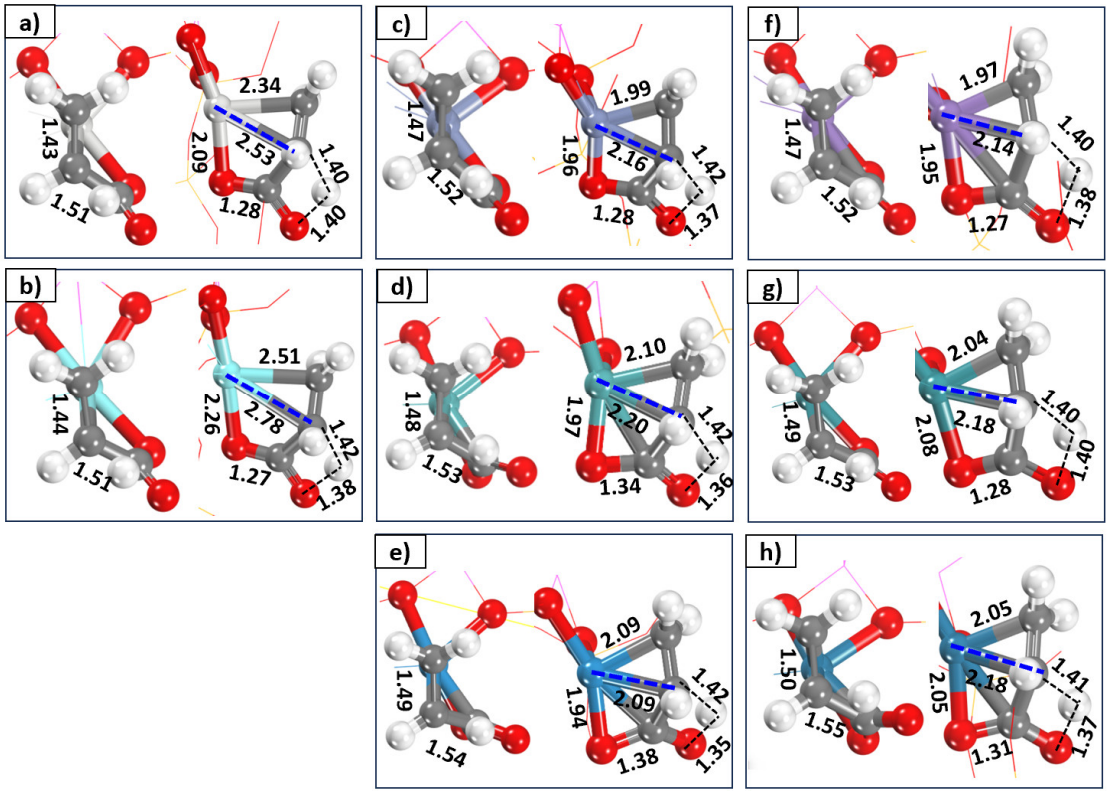

Figure 6. Structures of transition states (a) *Sc, (b) *Y, (c) *Cr, (d) *Mo (e) *W, (f) *Mn, (g) *Tc and (h) *Re. All bond distances are shown in Å. In each panel, the left sides show the top view and right-side shows the side view of transition state. MFI framework is indicated by lines. Blue dashed lines represent M–C(β–H) bond.

Activity descriptors based on electronic structure properties are highly desirable to reveal the fundamental reason behind the varied activity and predict catalyst performance. Here, we found that the kinetic barrier of β–H transfer and electronegativity (χ) have a reasonable correlation. **Figure 5(b)** shows that E_{act} is proportional to the electronegativity of the metal atom, indicating the transition state stabilization is affected by the electronegativity of the atom, though the β–H transfer is not occurring directly at the metal center. The less electronegative metal is desirable to stabilize the transition states more efficiently without driving significant charge redistribution (see

more detailed discussion below), hence facilitating β─H transfer. Additionally, Figure 5b suggests that the activation barrier is predominantly determined by the electronegativity, but the less linear trend than it in Figure 5a indicates other factors, such as the length of the reaction coordinates and local atomic structures, may also affect the activation barriers. In addition, the definition of electronegativity itself is quite complicated and necessitates a separate study.[59] Further insights can be gained through charge analysis, Bader charge analysis (**Table 2**) shows that on all metal centers, the β─H in the transition states carries a partial positive charge around +0.41 |e|. Over the more electronegative metal, this value of the positive charge slightly increases (**Figure S7**), causing more pronounced charge separation, which increases the activation barrier. Furthermore, the effect of electronegativity on β─H transfer was investigated by charge density difference analysis of metallalactone rings (**Figure 7**) using the equation $\Delta \rho = \rho(\text{MFI + metal + adsorbate}) - \rho(\text{MFI + metal}) - \rho(\text{adsorbate})$. **Figure 7a and b** (for metallalactone of *Sc and *Y) show minimal electron density inside the metallalactone ring as compared to other metals. Lack of electron accumulation inside the ring indicates reduced charge separation, allowing the proton transfer from β─C to oxygen, and is likely the main reason for lowering E_{act} of β─H transfer over *Sc and *Y.

Table 2. The activation energy for β─H transfer (E_{act}) (kJ/mol) and charge on β─H in the transition state.

M	Sc	Y	Cr	Mo	W	Mn	Tc	Re
E_{act}	119.6	129.3	168.8	181.4	193.0	139.9	177.5	188.1
Charge on β─H	0.36	0.36	0.42	0.43	0.43	0.40	0.42	0.42

Finally, we discuss the regeneration of the active centers, which is very important to sustain catalytic activity. The free energy change of the reaction $CO_{2(g)} + C_2H_{4(g)} \rightarrow C_2H_5COOH_{(l)}$ is 58.5 kJ/mol [60]. The stronger adsorption of $C_2H_{4(g)}$ on these metals can be utilized to regenerate the

catalysts. Excess supply of $C_2H_{4(g)}$ can displace adsorbed acrylic acid via ligand exchange method [61-62] (**Figure 2**, ΔG°_6). The adsorbed C_2H_4 can then start a new catalytic cycle. The ΔG°_6 to regenerate the active site via C_2H_4 adsorption are 71.4 kJ/mol for *Sc and 87.8 kJ/mol for *Y, respectively, comparable with other metal centers such as *Cr (53.1), *Mo (74.3), *W (51.1), *Mn (26.0), *Tc (73.3), and *Re (27.0). These moderate energy differences for ligand exchange are smaller than the activation barrier for the hydrogen transfer shown in Table 2, suggesting that the active sites can in principle be regenerated for the next catalytic cycle during the coupling reaction.

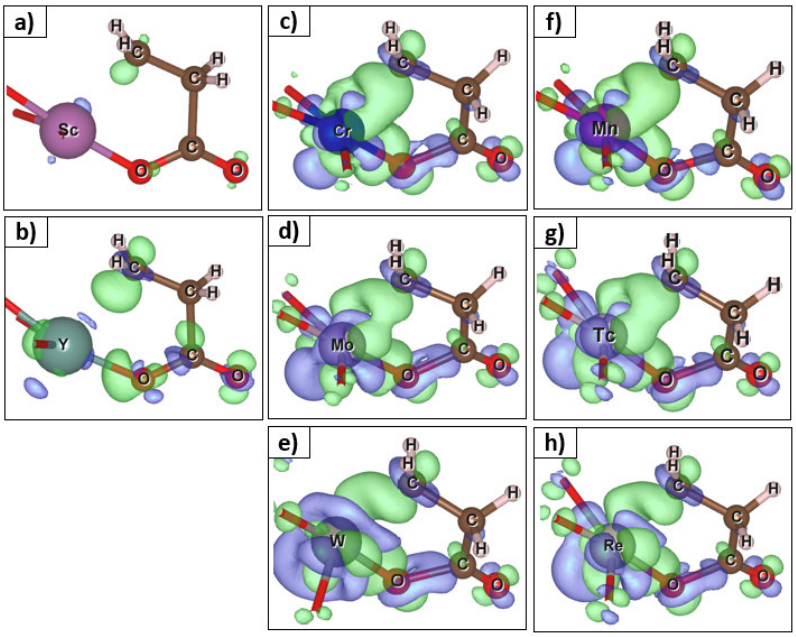

Figure 7. Charge density difference analysis of metallalactone of (a) *Sc, (b) *Y, (c) *Cr, (d) *Mo (e) *W, (f) *Mn, (g) *Tc and (h) *Re. Isosurfaces were drawn at isovalue of ± 0.01 e Å^{-3}. Green color shows accumulation of electron density and cyan color shows depletion of electron density. MFI framework was not shown for clarity.

It should be noted that this work adopted a simplified model with the same metal configuration and almost constant oxidation state to derive the mechanistic insights. However, strong adsorption of adsorbates on *Cr, *Re, *W and *Mo (Figure 4b) indicates the possibility of higher oxidation states of these metals and that maintaining 2+ oxidation state can be challenging. It is also anticipated that the oxidation state can be modified during experimental synthesis (by

controlling the Si/Al ratio) and evolve under the reaction conditions (e.g., by interacting with H, O, OH and other molecular ligands). It is thus valuable to explore, in future computational and experimental work, the dependence of the reaction profile as a function of metal centers with different oxidation states and ligands. In addition, acid- and base-assisted β─H transfer in molecular complexes was investigated in previous studies. [63-65] Base- or acid-assisted mechanisms were not considered here because we aimed to identify atom-efficient catalysts without the use of additional acid or base. [64, 66] There are alternate pathways in metal-exchanged MFI zeolites without introducing an additional acid or base, by hydrogen transfer mediated by the metal center [64, 66] or via oxygen in the MFI framework [66]. The metal-mediated hydrogen transfer was not likely to happen in MFI because the distance between H and metal was around 4 Å, too large for proton transfer. This transfer may be possible in molecular complexes because of the flexible nature of molecular complexes as compared to the rather rigid zeolite structure. The possibility of proton shuttling via adjacent framework oxygen was not investigated due to the similar distance (~4 Å) between H and the nearest O (from MFI).

Conclusions

Metal-exchanged zeolites can be prepared experimentally and provide an opportunity for designing the proposed active sites in a heterogeneous system. [10, 55] We show that atomically dispersed Sc, Y, Cr, Mo, W, Mn, Tc and Re in the MFI zeolites are the possible candidates for CO_2─ethylene coupling to produce acrylic acid due to favorable thermodynamics. We further investigated the kinetic barrier for the β─H transfer, which is likely the rate-limiting step, and showed that β─H transfer could be achieved with the moderate activation barriers over *Y and *Sc. Furthermore, we find that the electronegativity of metal centers has a qualitatively linear relation with the energy of activation for the β─H transfer. As the electronegativity of a metal

center decreases, the transition states become more stable likely due to reduced charge redistribution, and activation barriers are lowered. This study thus provides guidelines for designing zeolite-based catalysts for CO_2─ethylene coupling.

Conflicts of interest

There is no conflict of interest.

ORCID

Zaheer Masood: 0000-0003-2836-3754

Quy P. Nguyen: 0009-0006-0400-3868

Bin Wang: 0000-0001-8246-1422

Acknowledgment

The DFT calculations were performed at the OU Supercomputing Center for Education & Research and the National Energy Research Scientific Computing Center (NERSC), a U.S. Department of Energy Office of Science User Facility. The work was supported by the U.S. Department of Energy, Basic Energy Sciences, Chemical Sciences, Geosciences, and Biosciences (CSGB) Division, Catalysis Science (Grant DE-SC0023448).

Supporting Information

Structure and electronic properties of catalysts, optimized geometries of adsorbed C_2H_4 and metallalactone ring. Correlation of free energies of C_2H_4 with metallalactone and adsorbed acrylic

acid. Bader charges on atoms in metallalactone and transition states of β–H transfer. DOS of metal centers and C (β) in transition states.

References

1. Wang, X.; Wang, H.; Sun, Y., Synthesis of acrylic acid derivatives from CO2 and ethylene. *Chem* **2017,** *3* (2), 211-228.
2. Hollering, M.; Dutta, B.; Kühn, F. E., Transition metal mediated coupling of carbon dioxide and ethene to acrylic acid/acrylates. *Coord. Chem. Rev.* **2016,** *309*, 51-67.
3. Mori, H.; Müller, A. H., New polymeric architectures with (meth) acrylic acid segments. *Prog. Polym. Sci.* **2003,** *28* (10), 1403-1439.
4. Acrylic Acid Market Size, Share, Competitive Landscape and Trend Analysis Report by Derivative Type (Acrylic Esters, Acrylic Polymer, and Others), and End-User (Diapers, Surface Coatings Industry, Adhesives and Sealants Industry, Plastic Additives Industry, Water Treatment Industry, Textiles Industry, Surfactants Industry, and Others): Global Opportunity Analysis and Industry Forecast, 2021-2030. Allied Market Research, 2022. https://www.alliedmarketresearch.com/acrylic-acid-market#:~:text=Acrylic%20Acid%20Market%20Outlook%20%2D%202021,4.8%25%20from%202021%20to%202030. (accessed 2024-01-25).
5. NOJIRI, N.; SAKAI, Y.; WATANABE, Y., Two catalytic technologies of much influence on progress in chemical process development in Japan. *Catalysis Reviews* **1995,** *37* (1), 145-178.
6. Rodrigues, J. L., Heterologous Production of Acrylic Acid: Current Challenges and Perspectives. *SynBio* **2023,** *1* (1), 3-32.
7. Straathof, A. J.; Sie, S.; Franco, T. T.; Van der Wielen, L. A., Feasibility of acrylic acid production by fermentation. *Appl. Microbiol. Biotechnol.* **2005,** *67*, 727-734.
8. Murphy, B. M.; Mou, T.; Wang, B.; Xu, B., The effect of cofed species on the kinetics of catalytic methyl lactate dehydration on NaY. *ACS catal.* **2018,** *8* (10), 9066-9078.
9. Cauwenbergh, R.; Goyal, V.; Maiti, R.; Natte, K.; Das, S., Challenges and recent advancements in the transformation of CO2 into carboxylic acids: straightforward assembly with homogeneous 3d metals. *Chem. Soc. Rev.* **2022,** *51* (22), 9371-9423.
10. Velty, A.; Corma, A., Advanced zeolite and ordered mesoporous silica-based catalysts for the conversion of CO2 to chemicals and fuels. *Chem. Soc. Rev.* **2023,** *52* (5), 1773-1946.
11. Nathanael, A. J.; Kannaiyan, K.; Kunhiraman, A. K.; Ramakrishna, S.; Kumaravel, V., Global opportunities and challenges on net-zero CO2 emissions towards a sustainable future. *Reaction Chemistry & Engineering* **2021,** *6* (12), 2226-2247.
12. Davies, J.; Lyonnet, J. R.; Zimin, D. P.; Martin, R., The road to industrialization of fine chemical carboxylation reactions. *Chem* **2021,** *7* (11), 2927-2942.
13. Xiao, D. J.; Chant, E. D.; Frankhouser, A. D.; Chen, Y.; Yau, A.; Washton, N. M.; Kanan, M. W., A closed cycle for esterifying aromatic hydrocarbons with CO2 and alcohol. *Nature Chemistry* **2019,** *11* (10), 940-947.
14. Takahashi, K.; Sakurazawa, Y.; Iwai, A.; Iwasawa, N., Catalytic synthesis of a methylmalonate salt from ethylene and carbon dioxide through photoinduced activation and photoredox-catalyzed reduction of nickelalactones. *ACS catal.* **2022,** *12* (7), 3776-3781.
15. Vo, C. H.; Mondelli, C.; Hamedi, H.; Perez-Ramirez, J.; Farooq, S.; Karimi, I. A., Sustainability assessment of thermocatalytic conversion of CO2 to transportation fuels, methanol, and 1-propanol. *ACS Sustain. Chem. Eng.* **2021,** *9* (31), 10591-10600.

16. Pawar, A. U.; Kim, C. W.; Nguyen-Le, M.-T.; Kang, Y. S., General Review on the Components and Parameters of Photoelectrochemical System for CO2 Reduction with in Situ Analysis. *ACS Sustain. Chem. Eng.* **2019,** *7* (8), 7431-7455.
17. Wu, S.; Li, Y.; Hu, Q.; Wu, J.; Zhang, Q., Photothermocatalytic Dry Reforming of Methane for Efficient CO2 Reduction and Solar Energy Storage. *ACS Sustain. Chem. Eng.* **2021,** *9* (35), 11635-11651.
18. Chen, X.; Chen, J.; Alghoraibi, N. M.; Henckel, D. A.; Zhang, R.; Nwabara, U. O.; Madsen, K. E.; Kenis, P. J.; Zimmerman, S. C.; Gewirth, A. A., Electrochemical CO2-to-ethylene conversion on polyamine-incorporated Cu electrodes. *Nature Catalysis* **2021,** *4* (1), 20-27.
19. Lee, S. T.; Ghani, A. A.; D'Elia, V.; Cokoja, M.; Herrmann, W. A.; Basset, J.-M.; Kühn, F. E., Liberation of methyl acrylate from metallalactone complexes via M–O ring opening (M= Ni, Pd) with methylation agents. *New J. Chem.* **2013,** *37* (11), 3512-3517.
20. Alvarez, R.; Carmona, E.; Cole-Hamilton, D. J.; Galindo, A.; Gutierrez-Puebla, E.; Monge, A.; Poveda, M. L.; Ruiz, C., Formation of acrylic acid derivatives from the reaction of carbon dioxide with ethylene complexes of molybdenum and tungsten. *J. Am. Chem. Soc.* **1985,** *107* (19), 5529-5531.
21. Stieber, S. C. E.; Huguet, N.; Kageyama, T.; Jevtovikj, I.; Ariyananda, P.; Gordillo, A.; Schunk, S. A.; Rominger, F.; Hofmann, P.; Limbach, M., Acrylate formation from CO2 and ethylene: catalysis with palladium and mechanistic insight. *Chem. Commun.* **2015,** *51* (54), 10907-10909.
22. Graham, D. C.; Mitchell, C.; Bruce, M. I.; Metha, G. F.; Bowie, J. H.; Buntine, M. A., Production of Acrylic Acid through Nickel-Mediated Coupling of Ethylene and Carbon Dioxide—A DFT Study. *Organometallics* **2007,** *26* (27), 6784-6792.
23. Schubert, G.; Pápai, I., Acrylate Formation via Metal-Assisted C−C Coupling between CO2 and C2H4: Reaction Mechanism as Revealed from Density Functional Calculations. *J. Am. Chem. Soc.* **2003,** *125* (48), 14847-14858.
24. Hoberg, H.; Jenni, K.; Krüger, C.; Raabe, E., CC-Coupling of CO2 and Butadiene on Iron (0) Complexes—A Novel Route to α, ω-Dicarboxylic Acids. *Angewandte Chemie International Edition in English* **1986,** *25* (9), 810-811.
25. Al-Ghamdi, M.; Vummaleti, S. V. C.; Falivene, L.; Pasha, F. A.; Beetstra, D. J.; Cavallo, L., Structure–Activity Relationship To Screen Ni–Bisphosphine Complexes for the Oxidative Coupling of CO2 and Ethylene. *Organometallics* **2017,** *36* (6), 1107-1112.
26. Walther, D.; Dinjus, E., Aktivierung von Kohlendioxid an Übergangsmetallzentren; Die Metallaringschlußreaktion zwischen Kohlendioxid und 1, 3-Dienen am elektronenreichen Nickel (0)-Komplexrumpf. *Zeitschrift für Chemie* **1982,** *22* (6), 228-229.
27. Walther, D.; Dinjus, E.; Sieler, J.; Thanh, N. N.; Schade, W.; Leban, I., Aktivierung von CO2 an Übergangsmetallzentren: Struktur und Reaktivität eines CC-Kopplungsproduktes von CO2 und 2.3-Dimethylbutadien am elektronenreichen Nickel (O)/Activation of CO2 at Transition Metal Centers: Structure and Reactivity of a CC-Coupling Product of CO2 and 2, 3-Dimethylbutadiene at Electron-Rich Nickel (O). *Zeitschrift für Naturforschung B* **1983,** *38* (7), 835-840.
28. Hoberg, H.; Schaefer, D., Nickel (0)-induzierte c—c-verknüpfung zwischen alkenen und kohlendioxid. *J. Organomet. Chem.* **1982,** *236* (1), C28-C30.
29. Hoberg, H.; Schaefer, D.; Burkhart, G.; Krüger, C.; Romao, M., Nickel (0)-induzierte Cí C-verknüpfung zwischen kohlendioxid und alkinen sowie alkenen. *J. Organomet. Chem.* **1984,** *266* (2), 203-224.
30. Hoberg, H.; Ballesteros, A.; Sigan, A.; Jegat, C.; Milchereit, A., Durch (Lig) Ni (0) induzierte Herstellung von mono-und di-Carbonsäuren aus Cyclopenten und Kohlendioxid. *Synthesis* **1991,** *1991* (05), 395-398.
31. Hoberg, H.; Schaefer, D., Nickel (0)-induzierte Cí C-verknüpfung zwischen kohlendioxid und ethylen sowie mono-oder di-substituierten alkenen. *J. Organomet. Chem.* **1983,** *251* (3), c51-c53.
32. Hoberg, H.; Peres, Y.; Krüger, C.; Tsay, Y. H., A 1-Oxa-2-nickela-5-cyclopentanone from Ethene and Carbon Dioxide: Preparation, Structure, and Reactivity. *Angewandte Chemie International Edition in English* **1987,** *26* (8), 771-773.

33. Liu, X.; Wang, C.; Zhou, J.; Liu, C.; Liu, Z.; Shi, J.; Wang, Y.; Teng, J.; Xie, Z., Molecular transport in zeolite catalysts: depicting an integrated picture from macroscopic to microscopic scales. *Chem. Soc. Rev.* **2022,** *51* (19), 8174-8200.
34. Tang, B.; Li, S.; Song, W.-C.; Yang, E.-C.; Zhao, X.-J.; Guan, N.; Li, L., Fabrication of Hierarchical Sn-Beta Zeolite as Efficient Catalyst for Conversion of Cellulosic Sugar to Methyl Lactate. *ACS Sustain. Chem. Eng.* **2020,** *8* (9), 3796-3808.
35. Zong, R.; Li, H.; Ding, W.; Huang, H., Highly dispersed Pd on zeolite/carbon nanocomposites for selective hydrodeoxygenation of biomass-derived molecules under mild conditions. *ACS Sustain. Chem. Eng.* **2021,** *9* (29), 9891-9902.
36. Mullen, C. A.; Boateng, A. A., Production of aromatic hydrocarbons via catalytic pyrolysis of biomass over Fe-modified HZSM-5 zeolites. *ACS Sustain. Chem. Eng.* **2015,** *3* (7), 1623-1631.
37. Tu, C.; Nie, X.; Chen, J. G., Insight into Acetic Acid Synthesis from the Reaction of CH4 and CO2. *ACS catal.* **2021,** *11* (6), 3384-3401.
38. Rabie, A. M.; Betiha, M. A.; Park, S.-E., Direct synthesis of acetic acid by simultaneous co-activation of methane and CO2 over Cu-exchanged ZSM-5 catalysts. *Applied Catalysis B: Environmental* **2017,** *215*, 50-59.
39. Montejo-Valencia, B. D.; Pagán-Torres, Y. J.; Martínez-Iñesta, M. M.; Curet-Arana, M. C., Density functional theory (DFT) study to unravel the catalytic properties of M-exchanged MFI,(M= Be, Co, Cu, Mg, Mn, Zn) for the conversion of methane and carbon dioxide to acetic acid. *ACS catal.* **2017,** *7* (10), 6719-6728.
40. Graham, D. C.; Mitchell, C.; Bruce, M. I.; Metha, G. F.; Bowie, J. H.; Buntine, M. A., Production of Acrylic Acid through Nickel-Mediated Coupling of Ethylene and Carbon Dioxideí A DFT Study. *Organometallics* **2007,** *26* (27), 6784-6792.
41. Kresse, G.; Joubert, D., From ultrasoft pseudopotentials to the projector augmented-wave method. *Physical review b* **1999,** *59* (3), 1758.
42. Blöchl, P. E., Projector augmented-wave method. *Physical review B* **1994,** *50* (24), 17953.
43. Perdew, J. P.; Burke, K.; Ernzerhof, M., Generalized gradient approximation made simple. *Phys. Rev. Lett.* **1996,** *77* (18), 3865.
44. Kresse, G.; Furthmüller, J., Efficient iterative schemes for ab initio total-energy calculations using a plane-wave basis set. *Physical review B* **1996,** *54* (16), 11169.
45. van Koningsveld, H. v., High-temperature (350 K) orthorhombic framework structure of zeolite H-ZSM-5. *Acta Crystallogr. Sect. B: Struct. Sci.* **1990,** *46* (6), 731-735.
46. Chen, K.; Zornes, A.; Nguyen, V.; Wang, B.; Gan, Z.; Crossley, S. P.; White, J. L., 17O Labeling Reveals Paired Active Sites in Zeolite Catalysts. *J. Am. Chem. Soc.* **2022,** *144* (37), 16916-16929.
47. Chen, K.; Abdolrahmani, M.; Horstmeier, S.; Pham, T. N.; Nguyen, V. T.; Zeets, M.; Wang, B.; Crossley, S.; White, J. L., Brønsted–Brønsted Synergies between Framework and Noncrystalline Protons in Zeolite H-ZSM-5. *ACS catal.* **2019,** *9* (7), 6124-6136.
48. Grimme, S.; Antony, J.; Ehrlich, S.; Krieg, H., A consistent and accurate ab initio parametrization of density functional dispersion correction (DFT-D) for the 94 elements H-Pu. *J. Chem. Phys.* **2010,** *132* (15), 154104.
49. Grimme, S.; Ehrlich, S.; Goerigk, L., Effect of the damping function in dispersion corrected density functional theory. *J. Comput. Chem.* **2011,** *32* (7), 1456-1465.
50. Henkelman, G.; Uberuaga, B. P.; Jónsson, H., A climbing image nudged elastic band method for finding saddle points and minimum energy paths. *J. Chem. Phys.* **2000,** *113* (22), 9901-9904.
51. Henkelman, G.; Jónsson, H., A dimer method for finding saddle points on high dimensional potential surfaces using only first derivatives. *J. Chem. Phys.* **1999,** *111* (15), 7010-7022.
52. Wang, V.; Xu, N.; Liu, J.-C.; Tang, G.; Geng, W.-T., VASPKIT: A user-friendly interface facilitating high-throughput computing and analysis using VASP code. *Comput. Phys. Commun.* **2021,** *267*, 108033.
53. Grimme, S., Supramolecular Binding Thermodynamics by Dispersion-Corrected Density Functional Theory. *Chemistry – A European Journal* **2012,** *18* (32), 9955-9964.

54. Felvey, N.; Guo, J.; Rana, R.; Xu, L.; Bare, S. R.; Gates, B. C.; Katz, A.; Kulkarni, A. R.; Runnebaum, R. C.; Kronawitter, C. X., Interconversion of Atomically Dispersed Platinum Cations and Platinum Clusters in Zeolite ZSM-5 and Formation of Platinum gem-Dicarbonyls. *J. Am. Chem. Soc.* **2022,** *144* (30), 13874-13887.
55. Shamzhy, M.; Opanasenko, M.; Concepción, P.; Martínez, A., New trends in tailoring active sites in zeolite-based catalysts. *Chem. Soc. Rev.* **2019,** *48* (4), 1095-1149.
56. Zhang, R.; Song, L.; Liu, H.; Wang, B., The interaction mechanism of CO2 with CH3 and H on Cu (1 1 1) surface in synthesis of acetic acid from CH4/CO2: A DFT study. *Applied Catalysis A: General* **2012,** *443*, 50-58.
57. Zhao, Y.; Cui, C.; Han, J.; Wang, H.; Zhu, X.; Ge, Q., Direct C–C coupling of CO2 and the methyl group from CH4 activation through facile insertion of CO2 into Zn–CH3 σ-bond. *J. Am. Chem. Soc.* **2016,** *138* (32), 10191-10198.
58. Nørskov, J. K.; Bligaard, T.; Hvolbæk, B.; Abild-Pedersen, F.; Chorkendorff, I.; Christensen, C. H., The nature of the active site in heterogeneous metal catalysis. *Chem. Soc. Rev.* **2008,** *37* (10), 2163-2171.
59. Tantardini, C.; Oganov, A. R., Thermochemical electronegativities of the elements. *Nat. Commun.* **2021,** *12* (1), 2087.
60. Rummelt, S. M.; Zhong, H.; Korobkov, I.; Chirik, P. J., Iron-Mediated Coupling of Carbon Dioxide and Ethylene: Macrocyclic Metallalactones Enable Access to Various Carboxylates. *J. Am. Chem. Soc.* **2018,** *140* (37), 11589-11593.
61. Bruckmeier, C.; Lehenmeier, M. W.; Reichardt, R.; Vagin, S.; Rieger, B., Formation of Methyl Acrylate from CO2 and Ethylene via Methylation of Nickelalactones. *Organometallics* **2010,** *29* (10), 2199-2202.
62. Hoberg, H.; Peres, Y.; Milchereit, A., Cí C-Verknüpfund von alkenen mit CO2 an nickel (O); herstellung von zimtsäure aus styrol. *J. Organomet. Chem.* **1986,** *307* (2), C38-C40.
63. Li, G.; Wang, B.; Resasco, D. E., Solvent effects on catalytic reactions and related phenomena at liquid-solid interfaces. *Surf. Sci. Rep.* **2021,** *76* (4), 100541.
64. Limbach, M., Chapter Four - Acrylates from Alkenes and CO2, the Stuff That Dreams Are Made of. In *Adv. Organomet. Chem.*, Pérez, P. J., Ed. Academic Press: 2015; Vol. 63, pp 175-202.
65. Yang, G.; Schäffner, B.; Blug, M.; Hensen, E. J. M.; Pidko, E. A., A Mechanistic Study of Ni-catalyzed Carbon Dioxide Coupling with Ethylene towards the Manufacture of Acrylic Acid. *ChemCatChem* **2014,** *6* (3), 800-807.
66. Plessow, P. N.; Schäfer, A.; Limbach, M.; Hofmann, P., Acrylate Formation from CO2 and Ethylene Mediated by Nickel Complexes: A Theoretical Study. *Organometallics* **2014,** *33* (14), 3657-3668.

TOC Graphic
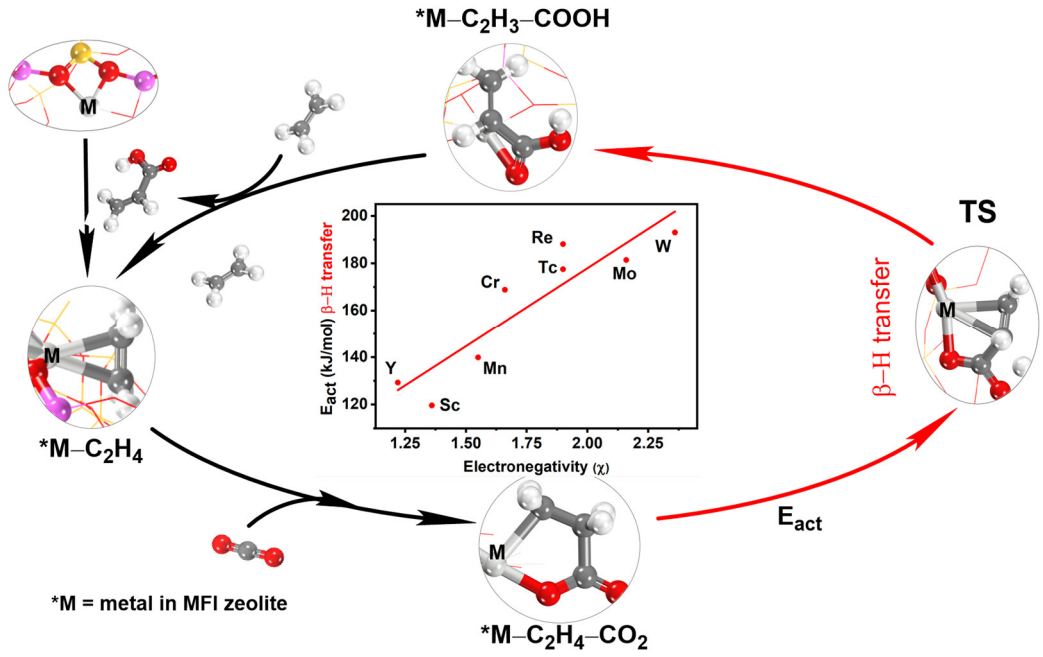
We report metal-exchange MFI zeolite as effecient catalysts for CO_2─Ethylene coupling to produce acrylic acid.